

Statistical analysis and modeling of the 3D morphology and texture of lunar regolith simulants

Matthias Weber^{a,*}, Ralf Ditscherlein^b, Lisa Ditscherlein^b, Tehya Birch^c,
Markus Franz^c, Achim Seidel^c, Urs A. Peuker^b, Orkun Furat^a, Volker
Schmidt^a, Georg Pöhle^d

^a*Institute of Stochastics, Ulm University, Helmholtzstr. 18, Ulm, 89081, Germany*

^b*Institute for Mechanical Process Engineering and Mineral Processing, TU Bergakademie
Freiberg, Agricolastr. 1, Freiberg, 09599, Germany*

^c*Airbus Defence and Space, Claude Dornier Str, Immenstaad, 88090, Germany*

^d*Fraunhofer Institute for Manufacturing Technology and Advanced Materials
IFAM, Winterbergstr. 28, Dresden, 01277, Germany*

Abstract

Understanding the mechanical behavior of lunar regolith under low-g conditions is essential for processing regolith in the lunar environment. While such mechanical properties are well understood for many granular materials on Earth, they have yet to be studied for lunar regolith. To derive a quantitative understanding of these mechanical properties such as rheology on Earth, regolith simulants are used in experiments, as they are synthesized to mimic certain physical or chemical aspects of lunar regolith. However, particle rheology is significantly influenced by particle size and shape. Yet, the size and shape of lunar regolith particles has not been thoroughly characterized. Moreover, it remains unclear how well simulant particles that are commonly used in experiments approximate the morphology of lunar regolith particles. In this paper, we quantify the multivariate (joint) distributions of size and shape descriptors of actual lunar regolith particles and seven commonly used regolith simulants using 3D tomographic image data obtained via micro computed tomography. The simulants include multiple variants designed to represent both mare- and highlands-type regolith. This analysis enables a systematic comparison of particle morphology across simulants and lunar

*Corresponding author

Email address: matthias.weber@uni-ulm.de (Matthias Weber)

samples. In particular, the quantitative analysis has confirmed that there are large differences in morphology within regolith simulants and between simulants and lunar regolith. This highlights the need to develop regolith simulants that approximate the morphology of lunar regolith for experimental investigations of size- and shape-dependent mechanical properties. An alternative would be the use of statistically representative digital models of lunar regolith particles as geometry input for numerical simulations, enabling systematic computer-based simulation studies of morphology-driven mechanical behavior under lunar conditions.

Keywords: 3D image data, X-ray micro-CT, regolith simulant, particle descriptor, parametric stochastic model

1. Introduction

Space exploration activities are expected to grow significantly over the next decades as evidenced by current trends and numerous roadmaps presented at national and global levels, beginning with the International Space Station and continuing to the lunar vicinity, the Moon, asteroids and Mars [1]. This trend is fueled by advancements in technology and, in particular, decreasing launch costs. Central to these ambitions is the concept of In-Situ Resource Utilization (ISRU), or “living off the land,” which emphasizes the production of essential resources such as oxygen and metals locally rather than supplying them from Earth. These resources are critical for life support, fuel production, construction, and other applications [1, 2]. ISRU activities are expected to grow to a market of 63 billion dollars by 2040, predominantly driven by oxygen production from local resources. The ROXY (Regolith to Oxygen and Metals Conversion) molten salt electrolysis process developed by Airbus meets the requirements for an economically viable ISRU process to extract oxygen and metals from regolith [1, 3, 4]. A lunar demonstration mission with a miniaturized version of a ROXY reactor, called Mini-ROXY, is currently in preparation [5].

As ISRU and lunar exploration efforts progress [6, 7], the handling and processing of lunar regolith will play a pivotal role. The Mini-ROXY mission exemplifies this focus as regolith handling involves significant challenges, including clogging and flow inconsistencies in transport and storage systems, which could jeopardize mission success. These issues arise from the unique and complex behavior of regolith under lunar conditions, where extreme tem-

perature variations, reduced gravity and electrostatic interactions influence its rheological and mechanical properties. One key objective of the Mini-ROXY lunar demonstration mission is therefore to improve our understanding of the behavior of lunar regolith in dynamical situations. This general approach, which has been coined UPREB (Universal Predictors of Regolith Behavior) [8], will help to fully exploit the potential of regolith for ISRU and further applications on the Moon and, with suitable adaptations, even beyond. The overarching question is how regolith behaves when being handled, mobilized, processed and transported on the lunar surface in partial gravity and in the lunar environment. Understanding these properties, namely, the rheology of lunar regolith, is crucial for predicting how regolith can be used for scientific extraction and ISRU.

Despite research progress [9, 10, 11, 12], substantial knowledge gaps remain in understanding the rheology of lunar regolith [13]. Large-scale experimental investigations of mechanical properties of regolith are currently unfeasible on the Moon and reproducing lunar conditions on the Earth requires elaborate experimental setups, e.g., parabolic flights or drop towers. Additionally, large quantities of lunar regolith are unavailable for mechanical experiments and while lunar regolith simulants exist, their applicability for such experiments is questionable.

In the past, the analysis of lunar regolith has focused on its chemical and mineralogical composition and properties [14, 15]. In order to mimic lunar regolith in that regard, various types of regolith simulants [16] have been developed. Additionally, mechanical properties of regolith simulants have been investigated [17]. However, it remains unclear whether regolith simulants are representative for lunar regolith with respect to their mechanical properties, as these are not only influenced by mineralogical properties but also by the size and shape of regolith particles. While these relationships are well understood for many granular materials and mechanical processes on Earth [18], the shapes of lunar regolith particles have only been analyzed for single [19] or a small number of particles in the past [20, 21]. Due to these concerns and constraints on experimental designs, regolith simulants may be insufficient to reliably predict the mechanical behavior of actual regolith under lunar conditions.

This gap may be bridged by numerical simulations applied to a digital twin of the 3D morphology and mineralogical composition of lunar regolith particles. Such a digital twin of lunar regolith can be obtained by stochastic 3D modeling of the shape and inner composition of regolith particles, based

on highly-resolved image data which are gained by computed tomography (CT). Investigating material properties by the combination of a digital twin and numerical simulations is known as virtual materials testing and has been successfully applied to various other materials [22, 23, 24]. For developing a realistic digital twin of lunar regolith, a better understanding of the 3D morphology and texture of lunar regolith particles is required.

In addition to the 2D characterization of statistically relevant quantities [25], 3D X-ray micro- and nano-CT measurements of large numbers of particles from samples of lunar regolith from the Apollo 11 and Apollo 14 missions [26] and, most recently, the Chang'e-5 mission [27], have only recently been performed and analyzed [28, 29]. In contrast to lunar regolith, many studies of regolith simulants are also limited to the investigation of a single regolith simulant [30] and therefore do not allow direct comparisons of inherent properties between different simulants.

In addition to the analysis of univariate descriptors of particle shape as discussed in [28], a multivariate analysis, incorporating information of chemical composition obtained from the raw CT data, will prove beneficial for a better understanding of regolith properties and behavior. In particular, it is well established for various other materials that their mechanical behavior on Earth typically depends on numerous influencing descriptors for their size, shape, surface roughness and composition [31]. For particle systems, these descriptors are typically random, making their characterization naturally suited to probability distributions. However, different types of descriptors are often correlated (e.g., when shape depends on size), meaning that describing them solely with univariate distributions results in a significant loss of information. To capture the full complexity of these interdependencies, it is essential to utilize multivariate probability distributions, which can account for the relationships and interactions among the descriptors, providing a more comprehensive and accurate statistical representation of the particle properties. Additionally, univariate or multivariate distributions of morphological particle descriptors are useful targets for the development of a digital twin for the 3D morphology of lunar regolith particles, i.e., for developing stochastic 3D models from which virtual, but realistic regolith particles can be generated for the purpose of virtual materials testing. While matching the precise shapes of individual particles could be considered overfitting of the stochastic 3D model, fitting of univariate distributions of individual morphological particle descriptors or, even better, multivariate distributions can be used for assessing the performance of a stochastic 3D model for particle

sizes, shapes and composition [32].

In the present paper, multivariate statistical analysis and parametric models for multivariate non-Gaussian probability distributions of descriptor vectors are used to better understand similarities and differences of regolith simulants particles. We apply these methods to 3D X-ray micro-CT data of different regolith simulants representing mare and highlands regolith. Additionally, we compare these simulants to three different samples of lunar regolith, highlighting the necessity for a thorough investigation of the shapes of lunar regolith particles to better understand their mechanical behavior.

2. Materials and Methods

In the following, we introduce the materials and methods used throughout this paper, including the regolith simulants, measurement techniques and considered particle descriptors.

2.1. Regolith Simulants

For analysis by X-ray CT, we chose four different mare and three different highland types of regolith simulants. Table 1 shows the different mineralogical compositions of these materials according to the manufacturer.

Table 1: Mineralogical composition (wt.%) of regolith simulants. The considered mineralogical phases, ordered from lowest to highest X-ray attenuation are: Plag = Plagioclase, Ol = Olivine, Px = Pyroxene, Bas = Basalt, Ilm = Ilmenite, m = Mare, h = Highland.

Name	Type	Glass	Plag	Ol	Px	Bas	Ilm
CSM-LHT-1	h	-	70.0	-	-	30.0	-
OB1A	h	43.2	44.4	6.3	0.6	-	-
LHS-1	h	24.2	74.4	0.2	0.3	0.5	0.4
JSC-1A	m	49.3	37.1	9.0	-	-	-
LMS-1	m	32.0	19.8	11.1	32.8	-	4.3
OPRL2N	m	90.0	10.0	-	-	-	-
CSM-LMT-1	m	-	-	10.0	-	86.0	4.0

For further analysis, in particular when using X-ray CT, only a limited range of particles sizes can be observed at the same time. Thus, in a first step, we chose to sieve all samples to $< 250 \mu m$. Table 2 shows information on the particle size distribution after sieving determined with laser diffraction

(Malvern, Mastersizer 3000). For the actual CT measurements, we additionally removed the fines below $25\ \mu\text{m}$ by wet sieving. Note that the size interval of the middle fraction from $25\ \mu\text{m}$ to $250\ \mu\text{m}$ is commonly used in other studies as well and is a trade-off between practical imaging constraints (like the minimum number of voxels for a reasonable description of particle shape). However, this selection may lead to bias. Finer and coarser particles often differ in shape and composition, which may affect the overall trends. Therefore, our results, and comparable studies as well, represent only part of the particle size distribution, and caution should be taken when generalizing. Following studies will include correlative measurements for evaluating excluded fractions.

Table 2: Mass density ρ , and quantiles q_{10}, q_{50}, q_{90} of the particle size distribution (sieved below $250\ \mu\text{m}$, determined with laser diffraction) for mare (m) and highland (h) regolith simulants, where the following abbreviations are used: CSM = Colorado School of Mines, EL = Exolith Lab, DI = Deltion Innovations Ltd., OPR = Off Planet Research.

Name	Type	Manufacturer	ρ (g/cm ³)	q_{10} (μm)	q_{50} (μm)	q_{90} (μm)
CSM-LHT-1	h	CSM	2.85	4.2	51.7	216.8
LHS-1	h	EL	3.30	9.9	82.9	234.7
OB1A	h	DI	3.03	18.9	80.3	185.2
JSC-1A	m	ORBITEC	2.90	18.1	74.9	233.2
LMS-1	m	EL	2.92	11.9	88.7	240.5
OPRL2N	m	OPR	2.85	3.8	31.2	156.5
CSM-LMT-1	m	CSM	2.90	4.7	54.8	206.7

2.2. Acquisition and Processing of Image Data

The acquisition and processing of image data considered in this paper consists of three steps: particle-discrete sample preparation, X-ray tomographic measurements, and data pre-processing and segmentation.

2.2.1. Particle-Discrete Sample Preparation

The basis for multivariate statistical data analysis is a set of particle-discrete morphological and textural descriptors of regolith simulants. To avoid time-consuming post-processing of image data prior to segmentation into individual particle volumes, an adapted sample preparation workflow was used that

keeps the regolith particles at a distance. Here, the well-known immobilization through epoxy embedding was complemented by introducing weakly X-ray absorbing carbon black spacer particles in the nanometer size range—much below the actual voxel resolution of $2.3 \mu\text{m}^3$ —to avoid agglomerates and sedimentation effects, which cannot be neglected in the present size and mass density range of the particles [33].

2.2.2. X-ray Tomographic Measurements

Non-destructive X-ray tomographic measurements have become a standard characterization method in recent years [34], especially when characterizing particulate systems [35]. A typical lab-based X-ray system uses a polychromatic source where electrons, accelerated from a cathode to a target anode (e.g., tungsten), generate X-rays. The interaction within the target creates a bulb-shaped volume, producing two types of X-rays. One of them are characteristic X-rays, determined by the target material, which are primarily useful for chemical analysis but irrelevant here, since the mineralogical composition of the target material is known. The other one is bremsstrahlung, a continuous spectrum influenced by filtering and electron acceleration voltage, which determines the main part of the integral spectrum used for the measurements. Here, the stability of the X-ray interaction bulb is critical for sharp and reproducible imaging. The conical X-ray beam passes through the sample, projecting onto a 2D flat panel detector. Unlike medical CT, the sample rotates while the detector remains fixed. Each rotational step produces a projection image, forming a series of 2D projection images to be processed into a 3D tomogram using reconstruction algorithms such as filtered back projection (FBP). For more details, we refer e.g. to [36]. Exemplary particles of the regolith simulants in Table 2 measured via X-ray tomography are visualized in Figure 1, where it is clearly visible that the particles show large variations in shape and surface modifications.

In order to make the measurements of the regolith simulant samples, i.e. their gray value distributions, as comparable as possible, the measurement parameters were kept constant (sample diameter: 2 mm, acceleration voltage: 80 keV, beam power: 7 W, exposure time: 1.5 s, binning: 2, filter: Zeiss standard LE4). Figure 2 shows exemplary slices from the seven regolith simulants.

A standardization of the gray values is needed to enable a quantitative analysis. This can only be done by utilizing correlative methods such as scanning electron microscopy (SEM) combined with energy-dispersive X-ray spec-

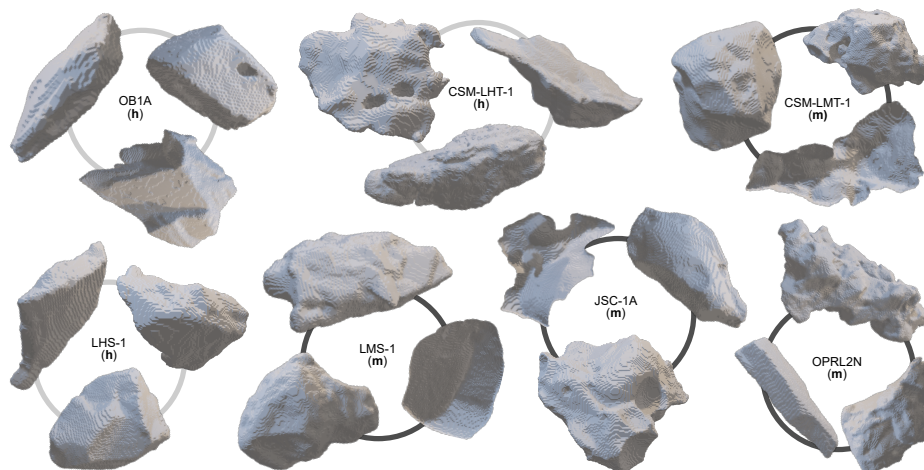


Figure 1: 3D models of selected particles ($150\mu\text{m}$ to $250\mu\text{m}$) from regolith simulants in Tab.2 illustrating the diversity in shape and surface texture. A scale bar is omitted, as the models are not rendered isometrically and are intended for qualitative visualization only.

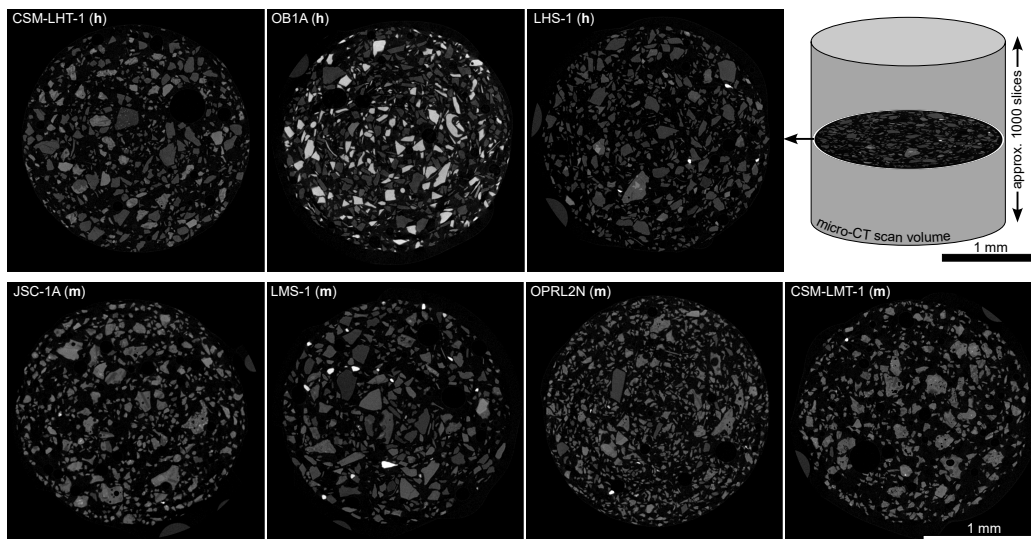


Figure 2: Exemplary slices of tomographically reconstructed samples of the regolith simulants in Table 2, measured via X-ray tomography. Highly X-ray attenuating phases are brighter, whereas less attenuating phases are darker. Spherical black areas are air bubbles due to the sample preparation procedure, which can later be used as markers for correlative scans.

troscopy (EDX), which is possible on the micrometer [37] and sub-micrometer scale [38]. However, these methods are limited to 2D measurements and cannot be carried out without further sample preparation. State-of-the-art spectral CT scanners can do this also in the 3D volume of the sample [39], but not yet with the resolution required here and, due to the large amount of data, not yet for a large number of densely packed samples with a large number of particles. To nevertheless create a valid starting point for gray value evaluation, all regolith samples were scanned and examined for the most highly absorbing phase, which represents the upper limit of the normalization condition. The other data sets were then reconstructed from the raw data within the new limits. Given a stable X-ray source and short consecutive measurements, the gray values can then be quantitatively compared with each other.

2.2.3. Data Pre-Processing and Segmentation

For discrete particle segmentation, a two-step supervised Ilastik training algorithm [40] was used, starting with the creation of a pixel classifier. In this step, the material phase is separated from the background phase (see Figure 3). In the next step, an automated routine processes the entire image stack, identifying individual volumes of the material phase and assigning them distinct colors. These color codes are then converted into unique gray values, referred to as labels, which are utilized in a second object-classifier routine to extract quantitative data. However, for particle-discrete analysis of the material phase distribution, it is crucial that the information about an aggregated gray value or histogram is preserved for each particle. This can be done by reusing the generated particle labels in combination with the original image data.

2.3. Particle Descriptors

The regolith simulants are analyzed with respect to different particle-discrete descriptors. In particular, descriptors of particle size and shape (Section 2.3.1) as well as such of texture (Section 2.3.2) are investigated, where the shapes of particles can be directly related to various rheological properties of bulk regolith like flowability, vulnerability to clogging and sieving behavior. Additionally, texture observed in CT images is analyzed as this relates to their chemical and mineralogical composition and, thereby, electrostatic properties. All particle descriptors considered in this paper are computed di-

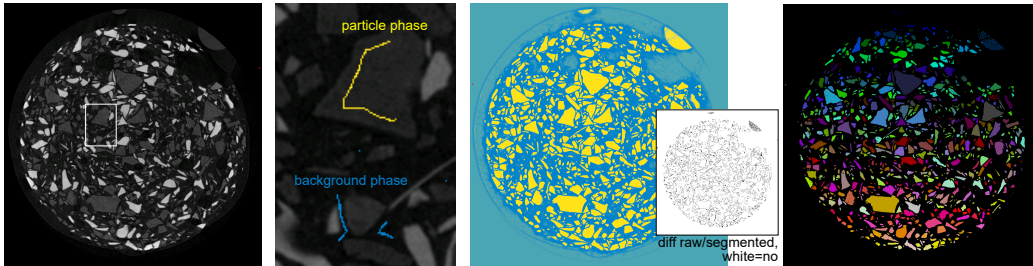


Figure 3: Exemplary reconstructed slice from the OB1A dataset with magnified region showing markers for the particle (yellow) and background phase (blue) to train the pixel-based classifier with Ilastik giving a segmented image (visual validation showing no missing particles) that can be used for an object-based classifier assigning a distinct false color map.

rectly from the voxelized image-data representation of particles stated in Section 2.2.

2.3.1. Morphological Descriptors

The most fundamental descriptors of particle morphology are the volume V and surface area A of a particle, where the particle volume is simply calculated by counting the voxels associated with that particle. The surface area is computed by the algorithm proposed in [41], which is based on a convolution of the image with a $2 \times 2 \times 2$ kernel and thus avoids the reconstruction of the actual surface while yielding more accurate results compared to simply counting voxels which touch both the interior and exterior of a particle. The latter would introduce a significant bias depending on the voxel-resolution of the measurement.

A commonly used descriptor of particle shape, being a measure of roundness, is the so-called sphericity S of a particle, which is given by

$$S = \frac{\pi(6V)^{2/3}}{3A} .$$

Additionally, the aspect ratio R of particles is considered, which is given as the ratio of the lengths of the longest and shortest principal axes of an ellipsoid with the same normalized second central moments as the particles. To compute the aspect ratio, the `measure.regionprops` method from the python package `scikit-image` [42] is used. Like sphericity, the aspect ratio R quantifies the roundness of particles, but is not affected by, e.g., surface roughness.

2.3.2. Textural Descriptors

As described in Section 2.2, the CT measurements of different simulants were performed with the aim of preserving comparability of gray values between different samples. Thus, besides morphological descriptors, meaningful descriptors of regolith particle texture can be computed for comparisons within and between simulants.

Since electrostatic charging, as one of the main phenomena of interest, is particularly related to the composition of particle surfaces, we split each particle into two parts: interior and surface. For this purpose, to avoid partial volume effects, we only consider voxels with a distance of more than $\sqrt{3}$ voxels ($\approx 4 \mu m$) to the boundary of particles. Then, all voxels with a distance between $\sqrt{3}$ and $2\sqrt{3}$ voxels to the particle boundary are considered as surface voxels, whereas voxels with a distance of more than $2\sqrt{3}$ voxels to the boundary are considered as interior voxels.

In the following, by G_s , G_i and G_t , the sets of gray values are denoted associated with surface, interior and all voxels of a particle, respectively, where the particle-wise mean gray value $\mu(G_x)$ and coefficient of variation $cv(G_x)$ are computed for each $x \in \{s, i, t\}$. Note that the quantities $\mu(G_s)$ and $\mu(G_i)$ are related with the average composition of the particle surface and interior, respectively, whereas $cv(G_s)$ and $cv(G_i)$ characterize the heterogeneity of these sub-volumes of a particle.

2.4. Stochastic Modeling of Particle Descriptor Vectors

To quantitatively compare the regolith simulants stated in Tables 1 and 2, we fit multivariate probability distributions to vectors of morphological and textural particle descriptors which have been introduced in Section 2.3. This is done in two steps. First, in Section 2.4.1, we consider univariate probability distributions of single particle descriptors. Then, in Sections 2.4.2 and 2.4.3, the univariate distributions are combined into a multivariate probability distribution of particle descriptor vectors, where the concept of copulas is used.

2.4.1. Univariate Distributions

A first step towards parametric modeling the (non-Gaussian) multivariate distributions of particle descriptor vectors is a parametric representation of the univariate distributions of individual descriptors. For this, we consider various parametric families of univariate probability distributions which can be fitted to the data, where the best-fitting distribution family is chosen

either among those implemented in the `scipy` package [43] or, alternatively, as a Gaussian mixture model. This choice of candidates may be adjusted, e.g., when prior knowledge about the expected distribution families is available for specific descriptors.

Two notable parametric distribution families which will be used in this paper are a version of the generalized inverse Gaussian distribution, whose probability density $f_{\text{gig}} : \mathbb{R} \rightarrow [0, \infty)$ can be defined as

$$f_{\text{gig}}(x; p, b) = x^{p-1} \exp(-b(x + 1/x)/2) / (2K_p(b)) \quad (1)$$

for each $x \in \mathbb{R}$ and some parameters $p \in \mathbb{R}, b > 0$, see [44], and the normal inverse Gaussian distribution with probability density $f_{\text{nig}} : \mathbb{R} \rightarrow [0, \infty)$ given by

$$f_{\text{nig}}(x; a, b) = \frac{a K_1(a\sqrt{1+x^2})}{\pi\sqrt{1+x^2}} \exp(\sqrt{a^2-b^2} + bx) \quad (2)$$

for each $x \in \mathbb{R}$ and some parameters $a > 0, |b| \leq a$, where $K_p : [0, \infty) \rightarrow [0, \infty)$ is a modified Bessel function of the second kind.

Note that the distribution families given in Eqs. (1) and (2) can be transformed linearly by additionally introducing so-called location and scale parameters $l \in \mathbb{R}$ and $s > 0$. For any probability density $f : \mathbb{R} \rightarrow [0, \infty)$, the transformed density $f_{l,s} : \mathbb{R} \rightarrow [0, \infty)$ is then given by $f_{l,s}(x) = f((x-l)/s)/s$ for each $x \in \mathbb{R}$.

Furthermore, as parametric model for a univariate bimodal distribution, we consider the Gaussian mixture model, whose probability density $f_{\text{GMM}} : \mathbb{R} \rightarrow [0, \infty)$ is given by

$$f_{\text{GMM}}(x; p, \mu_1, \mu_2, \sigma_1, \sigma_2) = p\varphi((x - \mu_1)/\sigma_1)/\sigma_1 + (1 - p)\varphi((x - \mu_2)/\sigma_2)/\sigma_2,$$

for each $x \in \mathbb{R}$, where $\varphi : \mathbb{R} \rightarrow [0, \infty)$ is the probability density of the standard normal distribution, $p \in [0, 1]$ is the mixing parameter, and $\mu_1, \mu_2 \in \mathbb{R}$ and σ_1, σ_2 are the mean values and standard deviations of the mixing components, respectively.

2.4.2. Archimedian Copulas

While the univariate distributions of single particle descriptors can be modeled by means of simple parametric distribution families, as stated in Section 2.4.1, the joint (multivariate) distributions of descriptor vectors in general do not follow an established modeling scheme like, e.g., a multivariate

Gaussian distribution. Thus, a more flexible approach is needed to model the joint distribution of particle descriptor vectors. So-called copulas [45] offer this flexibility by allowing to separately model the univariate (marginal) distributions and the correlation structure of a multivariate distribution.

For any fixed integer $d > 1$, a d -variate copula is the cumulative distribution function $C: [0, 1]^d \rightarrow [0, 1]$ of a d -dimensional random vector with uniform marginal distributions on $[0, 1]$. Furthermore, Sklar's representation formula [46, 45] motivates the use of copulas for the parametric modeling of (non-Gaussian) multivariate distributions, by stating that for any d -variate distribution function $F: \mathbb{R}^d \rightarrow [0, 1]$ with marginal distribution functions $F_1, \dots, F_d: \mathbb{R} \rightarrow [0, 1]$, there is a copula C such that

$$F(x_1, \dots, x_d) = C(F_1(x_1), \dots, F_d(x_d)), \quad (3)$$

for all $x_1, \dots, x_d \in \mathbb{R}$. Note that the formula given in Eq. (3) implies that the corresponding d -variate probability density $f: \mathbb{R}^d \rightarrow [0, \infty)$ can be given by

$$f(x_1, \dots, x_d) = c(F_1(x_1), \dots, F_d(x_d)) f_1(x_1) \dots f_d(x_d), \quad (4)$$

for all $x_1, \dots, x_d \in \mathbb{R}$, where $f_i: \mathbb{R} \rightarrow [0, \infty)$ is the (univariate) probability density corresponding to F_i for $i \in \{1, \dots, d\}$, and $c: [0, 1]^d \rightarrow [0, \infty)$ is the (d -variate) probability density corresponding to the copula $C: [0, 1]^d \rightarrow [0, 1]$.

Among other parametric copula families, so-called Archimedean copulas are often considered in the literature [46, 45]. For a continuous, strictly decreasing convex function $\psi: [0, 1] \rightarrow [0, \infty)$ with $\psi(1) = 0$, an Archimedean copula $C: [0, 1]^d \rightarrow [0, 1]$ is defined as

$$C(u_1, \dots, u_d) = \psi^{-1}(\psi(u_1) + \dots + \psi(u_d)), \quad (5)$$

for all $u_1, \dots, u_d \in [0, 1]$, where the function ψ on the right-hand side of Eq. (5) is called the generator function of the Archimedean copula and ψ^{-1} is the pseudo-inverse of ψ .

Two examples of Archimedean copulas which will be used in this paper are the so-called BB1 and BB8 copulas, as they turn out to best fit the data at hand. Their generators $\psi_{BB1}, \psi_{BB8}: [0, 1] \rightarrow [0, \infty)$ are given by

$$\psi_{BB1}(u; a, b) = (u^{-a} - 1)^b \quad (6)$$

and

$$\psi_{BB8}(u; \theta, \delta) = \log \left(\frac{1 - (1 - \delta u)^\theta}{1 - (1 - \delta)^\theta} \right), \quad (7)$$

for each $u \in [0, 1]$ and some parameters $a > 0, b \geq 1$ and $\theta \geq 1, 0 < \delta \leq 1$.

In the case of a bivariate copula $C: [0, 1]^2 \rightarrow [0, 1]$, so-called rotations $C_{90}, C_{180}, C_{270}: [0, 1]^2 \rightarrow [0, 1]$ of the copula C are defined for angles of 90° , 180° and 270° by $C_{90}(u_1, u_2) = C(u_2, 1 - u_1)$, $C_{180}(u_1, u_2) = C(1 - u_1, 1 - u_2)$ and $C_{270}(u_1, u_2) = C(1 - u_2, u_1)$ for any $u_1, u_2 \in [0, 1]$. For parametric copula families, allowing such rotations leads to a broader range of feasible copula structures.

2.4.3. R-Vine Copulas

Archimedean copulas, and an even wider range of other parametric copula families, are well-suited for modeling two-dimensional correlation structures. However, most of them fail to capture the complexity of higher-dimensional distributions. To overcome these limitations, so-called R-vine copulas [47, 46] have been developed that provide means of parametrically modeling multivariate distributions in arbitrary dimensions while providing increased flexibility to model the correlation structure.

R-vine copulas are based on the so-called pair-copula approach, which we outline for $d = 3$. Consider a three-dimensional random vector $X = (X_1, X_2, X_3)$ with joint probability density $f: \mathbb{R}^3 \rightarrow [0, \infty)$, marginal densities $f_1, f_2, f_3: \mathbb{R} \rightarrow [0, \infty)$ and corresponding (univariate) cumulative distribution functions $F_1, F_2, F_3: \mathbb{R} \rightarrow [0, 1]$. Using the notions of conditional probability densities and conditional cumulative distribution functions, the right-hand side of Eq. (4) can be re-written in the following form, see [48]: For all $(x_1, x_2, x_3) \in \mathbb{R}^3$ such that $f(x_1, x_2, x_3) > 0$, it holds that

$$\begin{aligned} f(x_1, x_2, x_3) &= c_{1,3|X_2=x_2}(F_{1|X_2=x_2}(x_1), F_{3|X_2=x_2}(x_3)) \\ &\quad \times c_{1,2}(F_1(x_1), F_2(x_2)) c_{2,3}(F_2(x_2), F_3(x_3)) f_1(x_1) f_2(x_2) f_3(x_3), \end{aligned} \quad (8)$$

where $c_{1,2}$ and $c_{2,3}$ are the copula densities corresponding to the distributions of (X_1, X_2) and (X_2, X_3) , respectively, and $c_{1,3|X_2=x_2}$ is that corresponding to the conditional distribution of (X_1, X_3) given that $X_2 = x_2$. Furthermore, $F_{i|X_2=x_2}$ denotes the conditional distribution function of X_i given that $X_2 = x_2$, for $i = 1, 3$. Usually, the simplifying assumption is made that $c_{1,3|2} = c_{1,3|X_2=x_2}$, i.e., the copula density $c_{1,3|X_2=x_2}$ does not depend on the specific value of X_2 , see [49]. Having in mind that

$$F_{1|X_2=x_2}(x_1) = \int_{-\infty}^{x_1} \frac{f_{1,2}(x, x_2)}{f_2(x_2)} dx = \int_{-\infty}^{x_1} c_{1,2}(F_1(x), F_2(x_2)) f_1(x) dx \quad (9)$$

and, analogously,

$$F_{3|X_2=x_2}(x_3) = \int_{-\infty}^{x_3} \frac{f_{2,3}(x_2, x)}{f_2(x_2)} dx = \int_{-\infty}^{x_2} c_{2,3}(F_2(x_2), F_3(x)) f_3(x) dx \quad (10)$$

for any $x_1, x_3 \in \mathbb{R}$, which follows from Eq. (4) with $d = 2$, the formula given in Eq. (8) yields a suitable approach for computing the joint probability density $f : \mathbb{R}^3 \rightarrow [0, \infty)$ of the three-dimensional random vector $X = (X_1, X_2, X_3)$, using (parametric) models for the (univariate) probability densities f_1 , f_2 and f_3 and the bivariate copula densities $c_{1,3|2}$, $c_{1,2}$ and $c_{2,3}$.

By iteratively applying the pair-copula approach stated above, representation formulas similar to that given in Eq. (8) can be obtained for any dimension $d > 3$, where d -variate probability densities are expressed by univariate probability densities and bivariate copula densities. However, since in the present paper only trivariate copula models will be used, we will not elaborate further on the general construction of R-vine copulas for arbitrary dimensions $d > 3$ and refer to [46, 47, 50, 51] for further details. For fitting (R-vine) copulas to data, we will make use of the `pyvinecopulib` package [52].

3. Results

The image data considered in Section 2.2 refers to 189504 individual particles of seven different regolith simulants. This data contains all segmented particles as discussed in Section 2.2. By computing the particle descriptors as outlined in Section 2.3, we obtain a dataset which forms the basis for the following statistical analysis of similarities and differences of regolith simulants.

3.1. Univariate Data Analysis

For putting the following analyses into perspective, recall that during sample preparation, fines below $25 \mu m$ and extremely large particles with sizes above $250 \mu m$ were removed which may change bulk properties compared to the specifications of manufacturers. Thus, the following analysis should be considered valid only for the measured fraction of particle sizes between $25 \mu m$ and $250 \mu m$.

We also remark that the probability densities used in the following, e.g., in Figures 5 and 6 are not volume-weighted and, therefore, they may not perfectly reflect the visual impression obtained from Figure 2.

Figure 4 shows the histograms of particle sizes as obtained by laser diffraction, in comparison to histograms of particle sizes computed from CT image data.

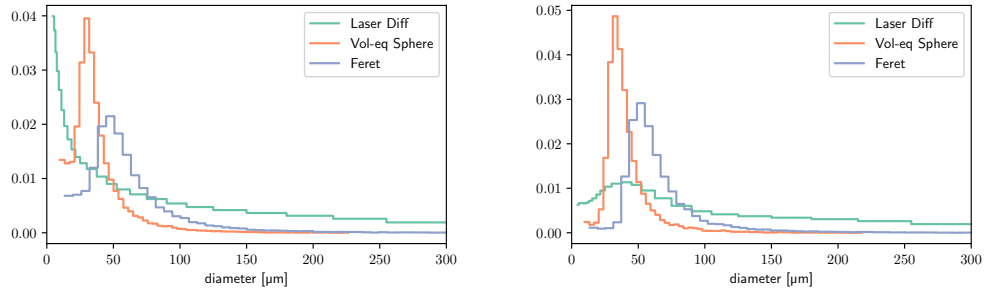


Figure 4: Histograms of particle sizes obtained for laser-diffraction data (green), for volume-equivalent spheres extracted from CT images (orange), and for feret diameters (blue), for the regolith simulants CSM-LHT-1 (left) and JSC-1A (right).

Some of the apparent differences between the histograms in Figure 4 may stem from the differences between the applied measurement techniques, a known issue when comparing results obtained from laser diffraction with those of CT image data [53]. However, in addition, different regolith simulants may contain hugely different amounts of fines which are present in the laser diffraction data but not in the samples used for CT imaging.

While measured samples and the original bulk material differ obviously with respect to the particle size distribution, further differences may exist which cannot be easily quantified.

In particular, Figure 5 visualizes probability densities of size and shape descriptors, whereas the corresponding probability densities of textural descriptors are shown in Figure 6.

Table 3 summarizes this analysis by providing the mean values of the probability densities shown in Figures 5 and 6 for all descriptors and simulants. As manufacturers specify regolith simulants with focus on different applications and, thus different compositions, it is not surprising that the mean values in the respective rows of Table 3 are quite different from each other, see Section 4.1 for a more detailed discussion.

3.2. Multivariate Data Analysis

While the data analysis performed in Section 3.1 was mainly focused on investigating similarities and differences between the distributions of single

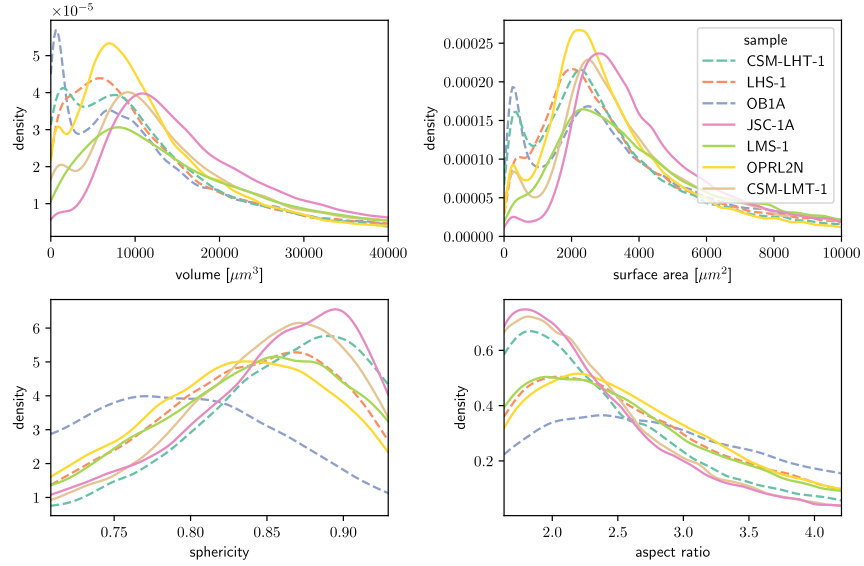


Figure 5: Estimated probability densities of particle volume, surface area, sphericity and aspect ratio. Highland simulants are shown as dashed lines, mare simulants as solid lines.

Table 3: Mean values of particle descriptors.

	highland			mare			
	CSM-LHT-1	LHS-1	OB1A	JSC-1A	LMS-1	OPRL2N	CSM-LMT-1
$V [\mu\text{m}^3]$	57906	51287	50990	55298	92874	31634	60802
$A [\mu\text{m}^2]$	6186	6235	7029	6846	9236	4900	6954
S	0.86	0.83	0.79	0.84	0.83	0.82	0.85
R	2.45	2.83	3.35	2.29	2.78	2.80	2.30
$\mu(G_{\text{interior}})$	11311	9966	15256	13691	11337	13313	13172
$\mu(G_{\text{surface}})$	11380	10186	14209	13313	10917	12925	12991
$\mu(G_{\text{total}})$	11355	10135	14285	13398	10995	12965	13023
$\text{cv}(G_{\text{interior}})$	0.07	0.06	0.06	0.08	0.07	0.07	0.08
$\text{cv}(G_{\text{surface}})$	0.08	0.07	0.08	0.10	0.09	0.09	0.09
$\text{cv}(G_{\text{total}})$	0.08	0.07	0.08	0.10	0.09	0.09	0.09
Particle number	25660	24819	33751	23923	16413	45372	19566

particle descriptors, this study shall also serve as a first step towards stochastic 3D modeling of regolith particles as mentioned in the introduction. To this end, a better understanding of the correlations between different descriptors

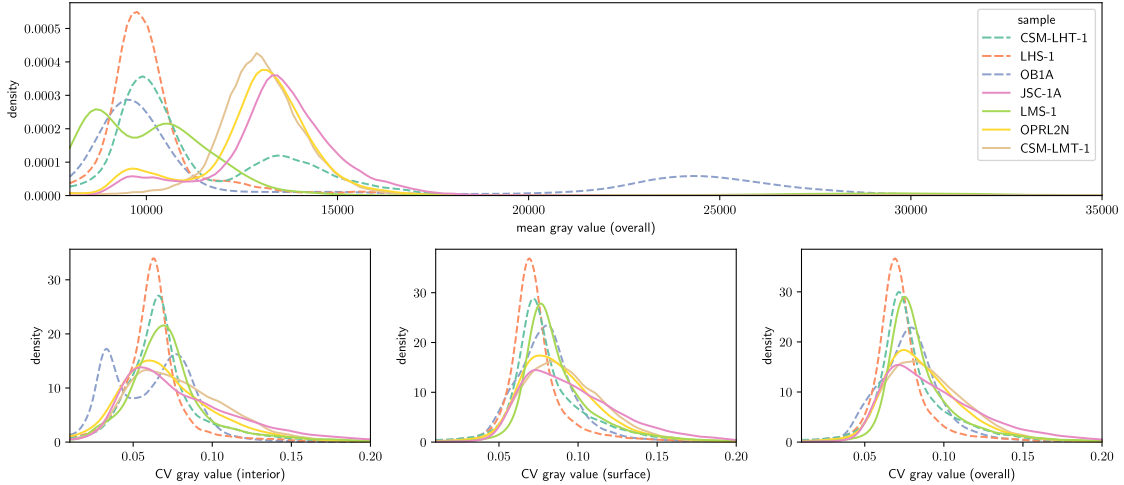


Figure 6: Top: Estimated probability densities of particle-wise mean gray values. Only the overall distributions are shown as there is no visible difference between them and the distributions for particle interior or surface. Bottom: Estimated probability densities of the coefficients of variation for particle interior, surface, and overall. Highland simulants are shown as dashed lines, mare simulants as solid lines.

and of their joint multivariate distributions is needed. We now demonstrate on the example of CSM-LHT-1 how these topics can be handled.

The Spearman rank correlation coefficients [46] of the pairs of particle descriptors given in Figure 7 show the expected behavior. In particular, the volumes and surface areas of particles are highly correlated. Aside from that, a strong negative correlation between volume (or surface area) and sphericity exists, suggesting that larger particles are less round. The aspect ratio, however, is not meaningfully correlated to neither volume nor surface area, so plate- or rod-shaped particles might come at all different sizes, see Section 4.2 for further discussions.

Figure 7 shows that many particle descriptors are correlated with each other. Thus, when investigating the morphology and texture of particles, bivariate distributions of two-dimensional descriptor vectors should be considered. In addition, in some cases, more than two descriptors should be considered simultaneously. For example, sphericity and mean gray value of CSM-LHT-1 particles are not strongly correlated ($r_s = 0.07$), but their joint distribution shows some kind of dependence with respect to the particle volume, as can be seen in Figure 8.

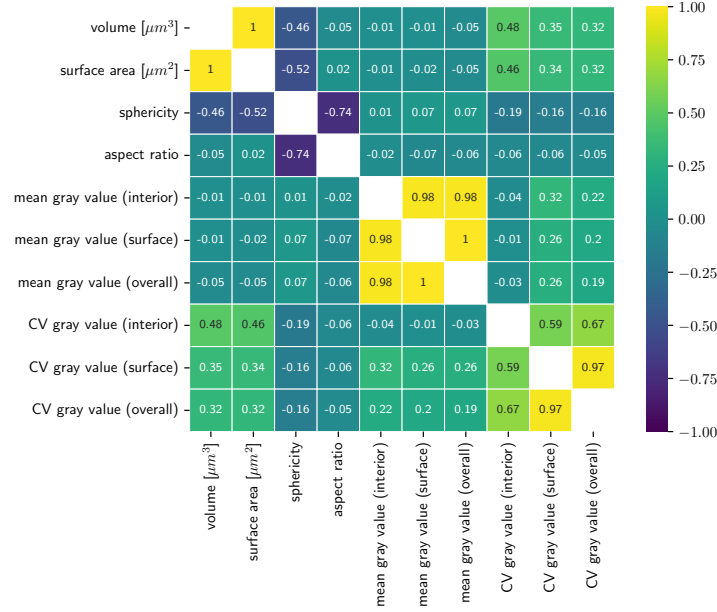


Figure 7: Spearman’s rank correlation coefficients, denoted by $r_s \in [-1, 1]$, for pairs of particle descriptors of CSM-LHT-1.

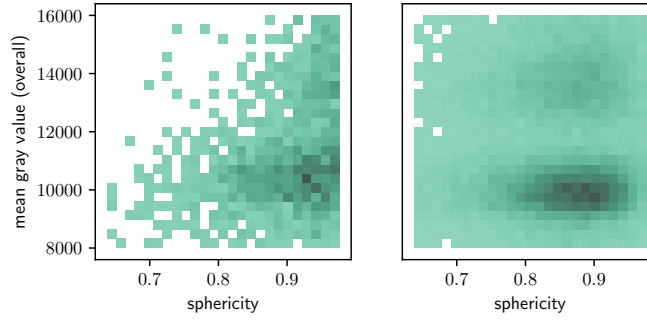


Figure 8: Histograms of the joint distribution of sphericity S and mean gray value $\mu(G_t)$ (overall) for two different numbers (denoted by n) of CSM-LHT-1 particles. Left: Particles with volume $V < 2600 \mu\text{m}^3$, $n = 2762$, $r_s = 0.35$. Right: All particles, $n = 24734$, $r_s = 0.07$.

3.3. Parametric Modeling of Univariate and Multivariate Distributions

To further investigate the behavior of particle descriptors of lunar regolith simulants, we parametrically model their univariate and multivariate probability distributions. In a forthcoming study, the resulting model parameters

will be used for the calibration and validation of stochastic 3D models of regolith simulant particles.

As can be seen from Figures 5 and 6, most univariate distributions of particle descriptors are not Gaussian, which implies that more sophisticated tools (than multivariate Gaussian distributions) are needed in order to parametrically model the multivariate distributions of descriptor vectors. In the following, we exemplarily show how the copula-based approach explained in Section 2.4 can be used to fit parametric bi- and trivariate distributions to descriptor vectors consisting of volumes, sphericities or/and mean gray values of CSM-LHT-1 particles.

In a first step, univariate parametric distributions are fitted to the data for each of these particle descriptors, as visualized in Figure 9, where the following procedure is used. For the volume V and sphericity S of CSM-LHT-1 particles, respectively, the best fitting type of a unimodal probability density is chosen among those parametric families of distributions implemented in the `scipy` package [43]. Furthermore, for the mean gray value $\mu(G_t)$ of CSM-LHT-1 particles, a Gaussian mixture model is considered. Recall that formulas for the univariate densities of these three types of parametric probability distributions have been stated in Section 2.4.1.

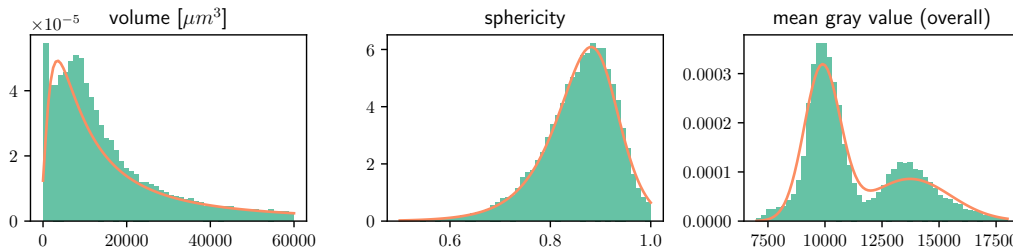


Figure 9: Fitted parametric probability densities for the volume V (left), sphericity S (middle) and mean gray value $\mu(G_t)$ (right) of CSM-LHT-1 particles.

It turned out that for the volume V and the sphericity S of CSM-LHT-1 particles the generalized inverse Gaussian distribution and the normal inverse Gaussian distribution, respectively, provide the best fits, see Figure 9. The optimal parameter values of these distributions are given in Table 4, which also contains the best fitting parameter values of the Gaussian mixture model for the mean gray value $\mu(G_t)$ of CSM-LHT-1 particles.

In the next step, we apply the pair-copula approach stated in Section 2.4.3 to model the the joint probability density $f : \mathbb{R}^3 \rightarrow [0, \infty)$ of the three-

Table 4: Types and optimal parameter values of the fitted univariate distributions.

descriptor	distribution type	optimal parameter values
V	gen. inv. Gaussian	$p = -0.99, b = 0.070,$ $l = -2059, s = 315450$
S	norm. inv. Gaussian	$a = 2.47$ $l = 0.91, s = 0.11$
$\mu(G_t)$	Gaussian mixture	$p = 0.38, \mu_1 = 13729, \mu_2 = 9879,$ $\sigma_1 = 1776, \sigma_2 = 792$

dimensional random vector $(X_1, X_2, X_3) = (V, S, \mu(G_t))$. For this, according to the representation formula for f given in Eq. (8), we need to determine the bivariate copulas $C_{1,3|2}$, $C_{1,2}$ and $C_{2,3}$ (resp. their densities $c_{1,3|2}$, $c_{1,2}$ and $c_{2,3}$), which we chose from the families of Gaussian, Clayton, Gumbel, Frank, Joe, BB1 and BB8 copulas [45, 46], using the pyvinecopulib package [52].

It turned out that the family of BB1 copulas provides the best fit for $C_{1,2}$ and $C_{2,3}$, whereas the family of BB8 copulas suits best for $C_{1,3|2}$. Note that both, BB1 and BB8, are Archimedean copulas, which have been introduced in Section 2.4.2. The optimal parameter values of these copulas are given in Table 5.

Table 5: Types and optimal parameter values of the fitted bivariate copulas.

descriptor pair	copula type	optimal parameter values	rotation
V, S	BB1	$a = 0.75, b = 1.07$	270°
$S, \mu(G_t)$	BB1	$a = 0.08, b = 1.01$	180°
$V, \mu(G_t) S$	BB8	$\theta = 1.09, \delta = 0.94$	270°

To validate the copula-based model given in Tables 4 and 5, we draw 10000 realizations from the fitted distribution of $(V, S, \mu(G_t))$ and visually compare resulting (bivariate) histograms to corresponding histograms of descriptor values computed from CT images. In particular, Figure 10 shows the bivariate histograms of measured data (top row) and model realizations (bottom row) for (V, S) in the left column, $(S, \mu(G_t))$ in the middle column, and $(S, \mu(G_t))$ conditional on $V < 2600 \mu m^3$ in the right column.

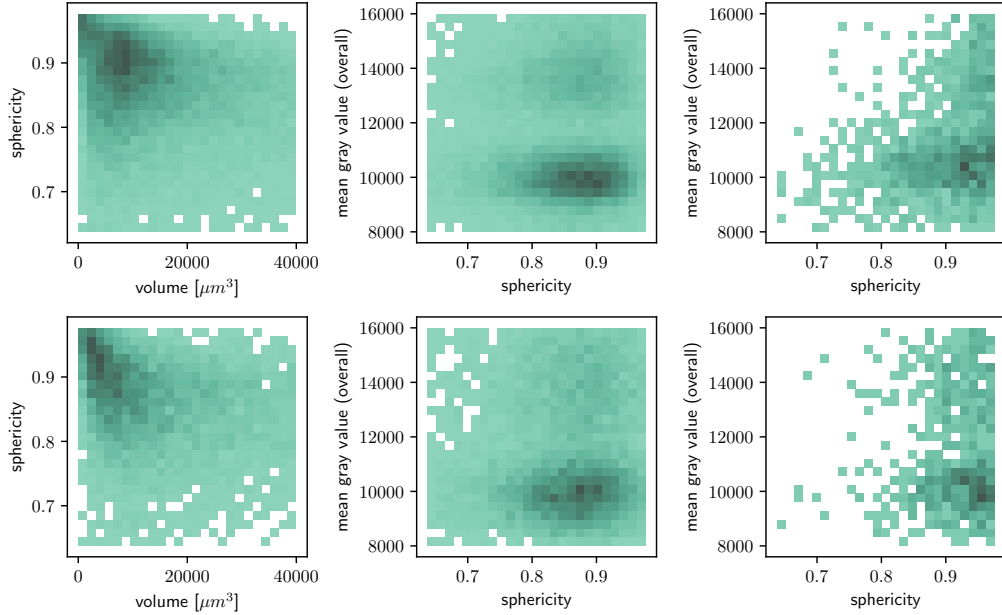


Figure 10: Bivariate histograms of measured data (top row) and simulated data drawn from the fitted copula-based model (bottom row), for CSM-LHT-1 particles. Left: Volume V v.s sphericity S . Middle: Sphericity S vs. mean gray value $\mu(G_t)$. Right: Sphericity S vs. mean gray value $\mu(G_t)$ given that $V < 2600 \mu m^3$, see also the histograms shown in Figure 8.

3.4. Comparison to Lunar Regolith

So far, the analysis showed significant differences between the considered regolith simulants with respect to various descriptors of shape and texture. To showcase differences between regolith simulants and actual lunar regolith, we additionally consider recently published 3D data of lunar regolith from Apollo samples 10084 and 14163 [26] and from the Chang’e-5 mission [27]. Note that for this analysis, we only consider particles with a volume larger than $15000 \mu m^3$ to avoid artifacts from segmentation, see also [27]. This roughly coincides with the lower limit of $25 \mu m$ diameter present for the measured regolith simulants.

Figure 11 shows the distributions of particle volume for all considered samples.

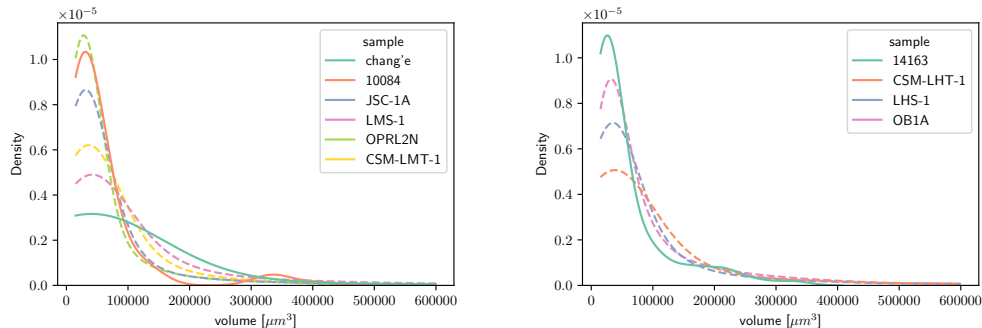


Figure 11: Comparison of estimated probability densities of particle volumes for lunar regolith (Apollo samples 10084, 14163 and Chang'e-5) and regolith simulants. Left: Mare samples. Right: Highlands samples.

4. Discussion

In this section we discuss the methods and results presented in this paper. In particular, Section 4.1 discusses the results of the univariate analysis, followed by a discussion of the multivariate analysis and model fits in Section 4.2. Then, Section 4.3 reflects on the implications of our findings in terms of comparability between different regolith simulants and lunar regolith.

4.1. Univariate Data Analysis

Notably, the rough shapes of the probability densities of volume, surface area, sphericity and aspect ratio shown in Figures 5 are similar for most simulants, where bimodal distributions can be observed for volume and surface area but not for sphericity and aspect ratio for all simulants except for LHS-1 and LMS-1. In general, highland simulants, shown as dashed lines in Figure 5, seem to contain a larger fraction of fine particles with low volume and surface area than mare simulants (solid lines). With respect to sphericity (and less so, aspect ratio), OB1A exhibits distinctly different particle shapes compared to all other simulants while the distributions of volume and surface area do not show this distinction. Particles of OB1A tend to be less spherical with a higher aspect ratio which may hint at more plate- or rod-shaped particles, which is in accordance with the visual impression from Figure 2.

Considering the distributions of mean gray values and the coefficients of variation of gray values, huge differences between the individual simulants can be observed, see Figure 6. Note that while the coefficient of variation is independent of the scale, the mean gray values (and individual voxel gray

values) lie between 0 and 65535, represented as 16-bit integers. Note that the distribution of the coefficients of variation for the gray values in the interior of OB1A particles is a kind of outlier, which is clearly bimodal and thus vastly different from those of all other simulants. In all other cases, the distributions of mean gray values and coefficients of variations of gray values do not differ considerably between particle surface and interior. Thus, in the following, we will not make this distinction and instead consider the overall gray value distributions.

With the exception of OB1A, as mentioned above, no clear differences can be seen in Figure 6 between the distributions of the coefficients of variation for the individual simulants. However, the distributions of mean gray values show pronounced similarities and differences. For most simulants, except LMS-1, the probability densities of mean gray values have peaks at either roughly 9000 or 13000, or both. This may hint at two main groups of constituents across all simulants.

Quantitatively, the heights of these peaks differ significantly between simulants, as shown in the top row of Figure 6. For example, most mare simulants, namely JSC-1A, OPRL2N and CSM-LMT-1, exhibit their major peak at roughly 13000. In addition, JSC-1A and OPRL2N show a minor peak at 9000. In contrast, the highland simulants LHS-1, CSM-LHT-1 and OB1A have their major peak at roughly 9000, with CSM-LHT-1 and OB1A exhibiting a secondary peak at roughly 13000 and 24000, respectively. On the other hand, LMS-1 shows an entirely different behavior with two peaks at around 8500 and 10800 where no peaks are located for the other simulants.

Although the mean values given in Table 3 cannot fully capture the information of the mostly bimodal distributions of the various particle descriptors, the main differences observed in Figures 5 and 6 are reflected in the mean values of Table 3. In particular, JSC-1A, OPRL2N and CSM-LMT-1 show (global) mean gray values near 13000, i.e., roughly at the same place where the major peaks of the corresponding particle-wise probability densities are located. Similarly, the peaks of the particle-wise probability densities of CSM-LHT-1 and LHS-1 are reflected in their global mean values. Notably, OB1A shows the highest mean gray value, heavily influenced by the secondary peak at 24000, visualized in the top row of Figure 6. Regarding descriptors of particle shape, the mean values of Table 3 roughly correspond to the visual impression of Figure 5. Notably, the mean values given in Table 3 for volume and surface area show that the tails of the corresponding particle-wise distributions are comparatively heavy, leading to mean values

significantly higher than the visually perceived peaks of the distributions.

4.2. Multivariate data analysis and parametric modeling

In this section, we discuss the results of the multivariate analysis and parametric modeling performed for CSM-LHT-1 particles, as presented in Sections 3.2 and 3.3. Figure 7 indicates that particle volume and surface area are strongly correlated, both negatively with sphericity, while aspect ratio exhibits no clear correlation with size-related descriptors, suggesting elongated particles occur across all sizes. Considering correlations between size and texture of particles, the coefficients of variation of particle-wise gray values are strongly positively correlated to particle sizes, i.e., volumes and surface areas of particles. This might indicate that larger particles are more likely to be composed of a mixture of different materials, which can also be observed in Figure 2. While further analysis of this behavior lies beyond the scope of the present paper, this could be reconsidered in a forthcoming study when trying to stochastically model the inner structure of particles. The fact that two or even more particle descriptors can be correlated is supported by the (conditional) bivariate histograms visualized in Figure 8, further, supporting the need of multivariately characterizing regolith particles, as performed in Section 3.3.

In particular, in Section 3.3, multivariate probability densities have been fitted to descriptor vectors by initially fitting parametric univariate marginal distributions, see Figure 9, followed by the deployment of parametric copulas to achieve bivariate fits, see Figure 10. As can be seen from Figure 10, the histograms of measured data (top row) are quite similar to the corresponding histograms of data simulated by the fitted copula-based model (bottom row), i.e., the copula-based model given in Tables 4 and 5 is indeed capable of capturing the empirical distributions of particle descriptor vectors computed from CT image data.

4.3. Regolith Simulant Comparability and Digital Modeling

As outlined in Section 1, understanding the mechanical properties of lunar regolith—especially under the conditions of reduced gravity and vacuum—is essential for enabling reliable regolith handling and processing during future lunar missions. Since experimental studies conducted under terrestrial conditions often use regolith simulants as substitutes for lunar regolith, it is equally interesting to understand how regolith simulants behave mechanically. However, the univariate analysis performed in Section 3.1 indicates

that regolith simulants that try to replicate the same type of lunar regolith (mare, highlands) differ significantly in terms of morphology and texture. However, since morphology and composition of particles also affect their mechanical properties, it is unclear to what extent the mechanical properties of the simulants under consideration are comparable to those of lunar regolith. While a detailed comparison with the lunar regolith considered in the present paper is difficult because the sample preparation, imaging and image processing steps used to collect the open source data of lunar regolith [28, 26, 27] do not necessarily correspond to the steps described in this paper, a basic comparison of particle size distribution already shows huge differences between regolith simulants and lunar regolith. Moreover, the distribution differs between lunar regolith from different landing sites, even for two mare landing sites from Apollo sample 10084 and the Chang’e mission. Bearing in mind that the lunar regolith samples have been measured and analyzed using different techniques, it is unclear to what extent these measured differences correspond to actual differences in material. These uncertainties together with the huge differences between regolith simulants and lunar regolith corroborate the need for further investigations of actual lunar regolith and the development of a digital twin for regolith from different landing sites.

For future comparisons of lunar regolith samples and regolith simulants, the parametric modeling performed in Section 3.3 can be employed as an efficient and systematic framework to quantify and compare the morphology and texture of different samples. In particular, this reduces complex 3D image data, of irregularly shaped particles, to relatively few interpretable parameters that characterize the multivariate probability distribution of descriptor vectors. Therefore, the comparison of different regolith samples can be reduced to a quantitative comparison of interpretable parameters.

Beyond characterization, the inferred multivariate distributions can be deployed for computer-based predictions of how different types of regolith behave as feed materials during processing operations. As demonstrated in related work on particle processing [54], the multivariate distribution of descriptor vectors influence bulk behavior and processing performance, further strengthening the case for digital, data-driven modeling approaches.

5. Conclusion and Outlook

In-Situ Resource Utilization (ISRU) plays a crucial role for future space exploration activities. A key aspect of ISRU is the production of oxygen from

locally available resources such as, e.g., the lunar regolith when planning long-term human presence on the moon. All approaches for utilizing lunar regolith, including the extraction of oxygen, require reliable mechanical handling of regolith. Compared to terrestrial applications, the lunar environment and special properties of lunar regolith pose extraordinary challenges when developing parts for regolith handling. Thus, a profound understanding of the rheology of lunar regolith is required for fast and reliable development of regolith handling equipment.

In the present paper, we took a first step towards a better understanding of mechanical properties of lunar regolith by outlining the methodology needed for understanding key aspects of regolith by CT imaging and subsequent statistical analysis of certain morphological and textural particle descriptors. Using this approach, we analyzed seven samples of different regolith simulants with respect to their size, shape and texture.

Although the various simulants exhibit some similarities, we found significant differences with respect to particle-wise texture (gray values) and, for some simulants, also with respect to particle shape. As it has been shown for other particulate materials that the (morphological and textural) descriptors of particles correlate with their behavior in mechanical processing, we may expect similar correlations for regolith simulants. In a forthcoming study, we plan to investigate these relationships in order to be able to predict the unknown behavior of lunar regolith under lunar conditions.

For these future investigations, we plan to measure the rheology of the same regolith simulants under near-lunar conditions in a parabolic flight facility. The methods and basic analyses established in the present paper will lay the foundation for correlating the behavior of regolith simulants in various experiments with their microstructure.

In addition to a descriptive statistical analysis of size, shape and texture of regolith simulant particles, we performed a multivariate analysis of particle descriptor vectors and parametrically modeled the joint distribution of three descriptors of size, shape and texture, using a copula-based modeling approach. This analysis and the capability to parametrically represent the joint distribution of an arbitrary number of particle descriptors may serve as a basis for the development of a stochastic 3D model for regolith particles.

In a forthcoming study, we will develop such a model to enable the in-silico analysis of different scenarios for better understanding how various aspects of regolith, specifications of regolith handling equipment and its effective behavior and performance are linked with each other. Then, in addition to

the development of a stochastic 3D model for regolith particles, this approach of virtual materials testing will also require some work on the calibration of numerical models for the particle behavior in mechanical processing to experimental data obtained from experiments performed under near-lunar conditions.

References

- [1] A. Seidel, M. Altenburg, E. Monchieri, F. Strigl, P. Quadbeck, C. Redlich, U. Pal, ROXY – An economically viable process to produce oxygen and metals from regolith, in: T. Leimkuehler, S. Macleod (Eds.), Proceedings of the 51st International Conference on Environmental Systems, 2022, iCES-2022-140.
- [2] K. C. Laurini, W. H. Gerstenmaier, The global exploration roadmap and its significance for NASA, *Space Policy* 30 (2014) 149–155.
- [3] M. Haeming, A. Seidel, U. Zell, Electrolysis apparatus for the electrolytic production of oxygen from oxide-containing starting material, uS11479869B2, 2020-10-12 (2020).
- [4] A. Seidel, U. B. Pal, P. Quadbeck, A. Adrian, Method and system for extracting metal and oxygen from powdered metal oxides, uS20230131891A1, 2021-10-25 (2021).
- [5] A. Seidel, E. Monchieri, U. Kübler, U. Pal, G. Pöhle, C. Redlich, A. Charitos, D. Vogt, T. Driebe, R. Grellmann, Mini-ROXY: The next step towards an efficient method for oxygen extraction from regolithy, Annual Meeting of the American Society for Gravitational and Space Research, 2023.
- [6] J. Deng, Y. Qian, F. Cui, Y. Liu, J. Lai, Research on lunar regolith of the Chang’e-4 landing site: An automated analysis method based on deep learning framework, *Icarus* 425 (2025) 116338.
- [7] L. Li, H. Hui, S. Hu, Q. Li, Y. Chen, W. Yang, G. Tang, L. Jia, X. Li, L. Gu, F. Wu, Discovery of carbonaceous chondritic fragment in Chang’e-5 regolith samples, *Icarus* 429 (2025) 116454.

- [8] T. Birch, A. Seidel, E. Monchieri, M. Franz, M. Weber, V. Schmidt, O. Furat, U. Peuker, R. Ditscherlein, L. Ditscherlein, C. Schilde, T. Lamping, G. Pöhle, C. Redlich, UPREB: Universal predictors of regolith behaviour -- concept and overview, in: S. Lapensee, M. Abney (Eds.), Proceedings of the 54th International Conference on Environmental Systems, 2022, iCES-2025-109.
- [9] M. Pourakbar, Y. Zhao, D. D. Cortes, S. Dai, Small-strain thermo-mechanical performance of lunar mare and highlands regolith simulants under Earth's atmospheric pressure and in vacuum, *Icarus* 429 (2025) 116405.
- [10] A. Tsuchiyama, H. Yamaguchi, M. Ogawa, A. M. Nakamura, T. Michikami, K. Uesugi, Abrasion experiments of mineral, rock, and meteorite particles: Simulating regolith particles abrasion on airless bodies, *Icarus* 429 (2025) 116432.
- [11] R. M. Tute, A. Goulas, Mechanical behaviour of sulphur-based martian regolith concrete processed under CO₂-rich conditions, *Icarus* 417 (2024) 116134.
- [12] P. Zanon, M. Dunn, G. Brooks, Lunar simulant behaviour variability and implications on terrestrial based lunar testing, *Icarus* 422 (2024) 116257.
- [13] M. Azami, Z. Kazemi, S. Moazen, M. Dubé, M.-J. Potvin, K. Skonieczny, A comprehensive review of lunar-based manufacturing and construction, *Progress in Aerospace Sciences* 150 (2024) 101045.
- [14] A. Martin, C. Wagoner, JHU-APL LSII REPORT: 2022 Lunar Simulant Assessment, Tech. rep., Johns Hopkins Applied Physics Laboratory, <https://lsic.jhuapl.edu/Our-Work/Working-Groups/files/Lunar-Simulants/2022%20Lunar%20Simulants%20Assessment%20Final.pdf>. Accessed: 2024-12-09 (2022).
- [15] L. Sibille, P. Carpenter, R. Schlagheck, R. A. French, Lunar regolith simulant materials: Recommendations for standardization, production, and usage, Tech. Rep. NASA/TP—2006–214605, <https://ntrs.nasa.gov/api/citations/20060051776/downloads/20060051776.pdf>. Accessed: 2024-09-12 (2006).

- [16] R. Li, G. Zhou, K. Yan, J. Chen, D. Chen, S. Cai, P.-Q. Mo, Preparation and characterization of a specialized lunar regolith simulant for use in lunar low gravity simulation, *International Journal of Mining Science and Technology* 32 (2022) 1–15.
- [17] H. Otto, K. Kerst, C. Roloff, G. Janiga, A. Katterfeld, CFD–DEM simulation and experimental investigation of the flow behavior of lunar regolith JSC-1A, *Particuology* 40 (2018) 34–43.
- [18] D. Schulze, *Powders and Bulk Solids*, Springer, 2021.
- [19] S. Baidya, M. Melius, A. M. Hassan, A. Sharits, A. N. Chiaramonti, T. Lafarge, J. D. Goguen, E. J. Garboczi, Optical scattering characteristics of 3–D lunar regolith particles measured using X–ray nano computed tomography, *IEEE Geoscience and Remote Sensing Letters* 19 (2022) 1–5.
- [20] J. Katagiri, T. Matsushima, Y. Yamada, A. Tsuchiyama, T. Nakano, K. Uesugi, M. Ohtake, K. Saiki, Investigation of 3D grain shape characteristics of lunar soil retrieved in Apollo 16 using image-based discrete-element modeling, *Journal of Aerospace Engineering* 28 (2015) 04014092.
- [21] A. Tsuchiyama, T. Sakurama, T. Nakano, K. Uesugi, M. Ohtake, T. Matsushima, K. Terakado, E. M. Galimov, Three-dimensional shape distribution of lunar regolith particles collected by the Apollo and Luna programs, *Earth, Planets and Space* 74 (2022) 172.
- [22] A. Jung, C. Redenbach, K. Schladitz, S. Staub, 3D image-based stochastic micro-structure modelling of foams for simulating elasticity, in: *Research in Mathematics of Materials Science*, Springer, 2022, pp. 257–281.
- [23] M. Neumann, O. Furat, D. Hlushkou, U. Tallarek, L. Holzer, V. Schmidt, On microstructure-property relationships derived by virtual materials testing with an emphasis on effective conductivity, in: M. Baum, G. Brenner, J. Grabowski, T. Hanschke, S. Hartmann, A. Schöbel (Eds.), *Simulation Science*, Springer International Publishing, Cham, 2018, pp. 145–158.
- [24] M. Weber, A. Grießer, D. Mosbach, E. Glatt, A. Wiegmann, V. Schmidt, Investigating microstructure–property relationships of nonwovens by

- model-based virtual material testing, *Transport in Porous Media* 151 (2024) 1403–1421.
- [25] M. Isachenkov, S. Chugunov, Z. Landsman, I. Akhatov, A. Metke, A. Tikhonov, I. Shishkovsky, Characterization of novel lunar highland and mare simulants for ISRU research applications, *Icarus* 376 (2022) 114873.
- [26] A. Chiaramonti, E. Garboczi, 3D shape and size data for 10084 and 14163 lunar regolith particles, national Institute of Standards and Technology. <https://doi.org/10.18434/mds2-3043>. Accessed: 2024-11-04 (2024).
- [27] H. Wu, Y. Zou, C. Zhang, W. Yang, B. Wu, K.-L. Yung, Q. Zhao, Micro-CT characterization of the Chang’e-5 Lunar regolith samples, *Journal of Geophysical Research: Planets* 130 (3) (2025) e2024JE008787.
- [28] J. Goguen, A. Sharits, A. Chiaramonti, T. Lafarge, E. Garboczi, Three-dimensional characterization of particle size, shape, and internal porosity for Apollo 11 and Apollo 14 lunar regolith and JSC-1A lunar regolith soil simulant, *Icarus* 420 (2024) 116166.
- [29] O. Kafka, N. Moser, A. Chiaramonti, E. Garboczi, R. Wilkerson, D. Rickman, Measurement of the three-dimensional shape and size distribution of 17 lunar regolith simulants: Simulant shape and size inter-comparison and simulant shape comparison with Apollo 11 and Apollo 14 lunar regolith, *Icarus* 434 (2025) 116542.
- [30] B. Peng, R. Hay, K. Celik, 3D shape analysis of lunar regolith simulants, *Powder Technology* 426 (2023) 118621.
- [31] A. Spetl, M. Dosta, S. Bachstein, S. Heinrich, V. Schmidt, Microstructural effects in breakage behavior of real and virtual agglomerates under compressive load: Automated extraction of internal microstructures, their stochastic modeling and copula-based breakage models fitted to DEM data, in: *Proceedings of the International Congress on Particle Technology, Nürnberg, 2016*, paper-ID 1.18.
- [32] B. Prifling, D. Westhoff, D. Schmidt, H. Markoetter, I. Manke, V. Knoblauch, V. Schmidt, Parametric microstructure modeling of com-

- pressed cathode materials for li-ion batteries, *Computational Materials Science* 169 (2019) 109083.
- [33] R. Ditscherlein, T. Leißner, U. A. Peuker, Preparation strategy for statistically significant micrometer-sized particle systems suitable for correlative 3D imaging workflows on the example of X-ray microtomography, *Powder Technology* 395 (2022) 235–242.
- [34] P. J. Withers, C. Bouman, S. Carmignato, V. Cnudde, D. Grimaldi, C. K. Hagen, E. Maire, M. Manley, A. du Plessis, S. R. Stock, X-ray computed tomography, *Nature Reviews Methods Primers* 1 (2021) 18.
- [35] C. L. Lin, J. D. Miller, 3D characterization and analysis of particle shape using X-ray microtomography (XMT), *Powder Technology* 154 (1) (2005) 61–69.
- [36] T. M. Buzug, *Computed Tomography: From Photon Statistics to Modern Cone-Beam CT*, Springer, 2008.
- [37] B. Schulz, D. Sandmann, S. Gilbricht, SEM-based automated mineralogy and its application in geo- and material sciences, *Minerals* 10 (2020) 1004.
- [38] S. Englisch, R. Ditscherlein, T. Kirstein, L. Hansen, O. Furat, D. Drobek, T. Leißner, B. Apeleo Zubiri, A. P. Weber, V. Schmidt, U. A. Peuker, E. Spiecker, 3D analysis of equally X-ray attenuating mineralogical phases utilizing a correlative tomographic workflow across multiple length scales, *Powder Technology* 419 (2023) 118343.
- [39] J. Sittner, J. R. Da Assuncao Godinho, A. Renno, V. Cnudde, M. Boone, T. de Schryver, D. van Loo, M. Merkulova, A. Roine, J. Liipo, Spectral X-ray computed micro tomography: 3-dimensional chemical imaging, *X-Ray Spectrometry* 50 (2020) 92–105.
- [40] S. Berg, D. Kutra, T. Kroeger, C. N. Straehle, B. X. Kausler, C. Haubold, M. Schiegg, J. Ales, T. Beier, M. Rudy, K. Eren, J. I. Cervantes, B. Xu, F. Beuttenmueller, A. Wolny, C. Zhang, U. Koethe, F. A. Hamprecht, A. Kreshuk, *ilastik: interactive machine learning for (bio)image analysis*, *Nature Methods* 16 (2019) 1226—1232.

- [41] K. Schladitz, J. Ohser, W. Nagel, Measuring intrinsic volumes in digital 3D images, in: A. Kuba, L. Nyúl, K. Palágyi (Eds.), 13th International Conference on Discrete Geometry for Computer Imagery, Springer, 2007, pp. 247–258.
- [42] S. Van der Walt, J. L. Schönberger, J. Nunez-Iglesias, F. Boulogne, J. D. Warner, N. Yager, E. Gouillart, T. Yu, scikit-image: Image processing in python, *PeerJ* 2 (2014) e453.
- [43] P. Virtanen, R. Gommers, T. E. Oliphant, M. Haberland, T. Reddy, D. Cournapeau, E. Burovski, P. Peterson, W. Weckesser, J. Bright, S. J. van der Walt, M. Brett, J. Wilson, K. J. Millman, N. Mayorov, A. R. J. Nelson, E. Jones, R. Kern, E. Larson, C. J. Carey, Í. Polat, Y. Feng, E. W. Moore, J. VanderPlas, D. Laxalde, J. Perktold, R. Cimrman, I. Henriksen, E. A. Quintero, C. R. Harris, A. M. Archibald, A. H. Ribeiro, F. Pedregosa, P. van Mulbregt, SciPy 1.0 Contributors, SciPy 1.0: Fundamental algorithms for scientific computing in python, *Nature Methods* 17 (2020) 261–272.
- [44] O. Barndorff-Nielsen, P. Blæsild, C. Halgreen, First hitting time models for the generalized inverse gaussian distribution, *Stochastic Processes and their Applications* 7 (1) (1978) 49–54.
- [45] R. B. Nelsen, *An Introduction to Copulas*, Springer, 2006.
- [46] H. Joe, *Dependence Modeling with Copulas*, Chapman and Hall/CRC, 2014.
- [47] C. Czado, *Analyzing Dependent Data with Vine Copulas*, Springer, 2019.
- [48] M. Weber, A. Griebner, E. Glatt, A. Wiegmann, V. Schmidt, Modeling curved fibers by fitting R-vine copulas to their frenet representations, *Microscopy and Microanalysis* 29 (2022) 155–165. arXiv:<https://academic.oup.com/mam/article-pdf/29/1/155/49033932/ozac030.pdf>.
- [49] I. H. Haff, K. Aas, A. Frigessi, On the simplified pair-copula construction—simply useful or too simplistic, *Journal of Multivariate Analysis* 101 (2010) 1296–1310.

- [50] K.-M. Aigner, P. Schaumann, F. v. Loeper, A. Martin, V. Schmidt, F. Liers, Robust DC optimal power flow with modeling of solar power supply uncertainty via R-vine copulas, *Optimization and Engineering* 24 (2023) 1951–1982.
- [51] O. Furat, T. Kirstein, T. Leißner, K. Bachmann, J. Gutzmer, U. A. Peuker, V. Schmidt, Multidimensional characterization of particle morphology and mineralogical composition using CT data and R-vine copulas, *Minerals Engineering* 206 (2024) 108520.
- [52] Vinecopulib, Vinecopulib/pyvinecopulib: A python library for vine copula models, <https://github.com/vinecopulib/pyvinecopulib>, accessed: 2023-04-20 (2023).
- [53] S. T. Erdoğan, E. T. Garboczi, D. W. Fowler, Shape and size of microfine aggregates: X-ray microcomputed tomography vs. laser diffraction, *Powder Technology* 177 (2007) 53–63.
- [54] O. Furat, M. Masuhr, F. E. Kruijs, V. Schmidt, Stochastic modeling of classifying aerodynamic lenses for separation of airborne particles by material and size, *Advanced Powder Technology* 31 (6) (2020) 2215–2226.